In-depth analysis of defects in TiO_2 compact electron transport layers and impact on performance and hysteresis of planar perovskite devices at low light.

Anthony Lewis, Joel R. Troughton, Benjamin Smith, James McGettrick, Tom Dunlop, Francesca De Rossi, Adam Pockett, Michael Spence, Matthew J. Carnie, Trystan M. Watson, Cécile Charbonneau*

*Corresponding author

SPECIFIC-IKC, Swansea University, Department of Materials Engineering
Engineering East, Swansea University Bay Campus, Crymlyn Burrows, Swansea, SA1 8EN

Abstract

Properties of the electron transport layer (ETL) are known to influence the performance of lead halide perovskite solar cells (PSCs). But so far very little emphasis has been given on the increased impact of this layer at low light. In this work we compare the effect of thickness and coverage of a TiO_2 compact layer on the performance and hysteresis of standard methyl ammonium lead iodide planar devices tested under 200 lux vs. 1 sun illumination. Standard TiO_2 layers are produced with incremental thickness and coverage by application of spray pyrolysis of a Ti-acetylacetonate precursor (0-50 sprays, 1 spray ~ 1 nm TiO_2). Thorough materials characterisation combining FEG-SEM, XPS, and cyclic voltammetry shows that a crystalline, nearly pin-hole free TiO_2 layer is achieved by sequential deposition of ≥ 15 sprays over small to large areas (0.2 mm^2 – 1 cm^2). Device performance is affected by two main parameters, namely the coverage yield and thickness of the TiO_2 layer, especially under 200 lux illumination. A 25 vs. 50 sprays-TiO_2 layer is found to provide the best compromise between coverage and thickness to avoid charge recombination at the TiO_2/perovskite interface whilst minimizing resistive losses with 11.7 % average PCE at 200 lux vs 7.8 % under 1 sun. Finally, the analysis of I/V forward vs. reverse scans and open circuit voltage decay data suggests that hysteresis is greatly affected by the capacitive properties of the ETL at low light, whilst other phenomena such as ion migrations may dominate under 1 sun.

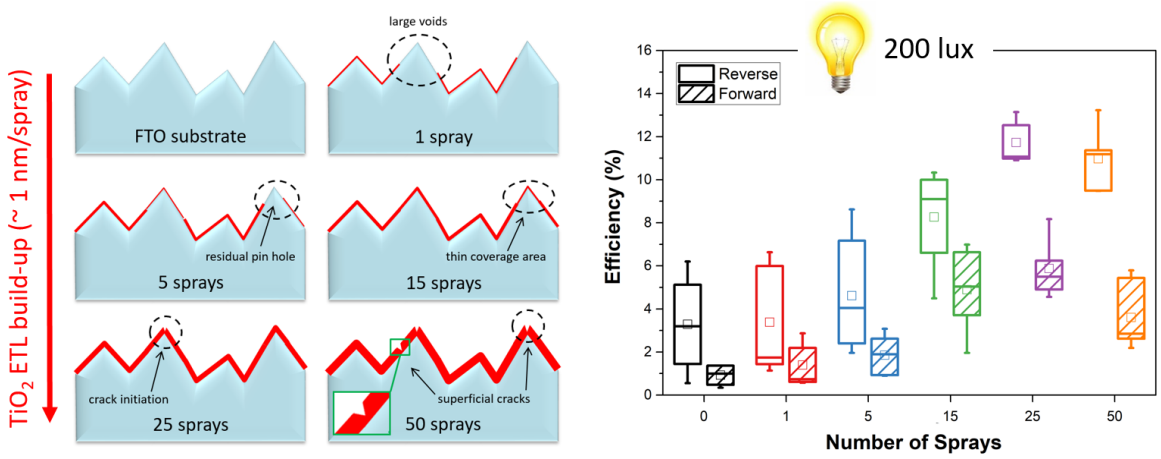

Introduction

Following the emergence of organo-metallic perovskite photovoltaic (PV) solar cells [1,2], continuous improvements in device performance (now up to 24.2% PCE certified by NREL in 2019 [3]) and stability [4] have been reported across a rapidly expanding community of research groups. Perovskite solar cells (PSCs) are now expected to make a real impact in the future of the global solar market [5]. Whilst successful combinations of materials and device architectures multiply [6], strategic choices are being made by research teams and start-ups focusing on scaling-up the fabrication of PSC devices [7–11]. These choices are also influenced by the compatibility of manufacturing processes already available and the destination of PSC photovoltaic-powered products. Indeed, thanks to continuous improvements in device stability, PSCs are now prognosticated a bright future as outdoor building integrated photovoltaics where Si-PV can't be adopted. In addition, there is increasing interest in using PSCs to power indoor technologies [8,12–15]. PSCs have been shown to perform very well at low light, with efficiency often reported above 25% and high voltage output in standalone devices, matching assets developed in other 3rd generation photovoltaic systems such as OPVs [16] and dye-sensitized solar cells [17].

Years of research on the development of 3rd generation photovoltaic devices have encouraged scientists to build devices by sequential deposition of stacked layers of semiconductor materials contained between two conductive electrodes. The most basic version of the stack consists of 3 planar layers: first an electron collector/transport layer (ETL) is prepared on the anodic substrate, followed by a light-absorber, and a hole transport layer (HTL) topped by metallic back contacts. Planar device structures have been adopted by many research groups leading small and large scale PSC research activities; although not record-holders, planar devices have reached relatively stable outputs of 18% and above [18,19]. The ETL often consists of a thin layer of compact crystalline TiO_2, a material with good chemical stability and semiconductor properties compatible with the extraction of electrons generated by many types of organo-metal halide perovskites. Many other materials have been considered for the fabrication of ETLs [20] such as PCBM, CdSe quantum-dot modified PCBM [21], SnO_2 and ZnO which are attractive because they can be processed at low-temperature on flexible ITO-PET substrates [22]. However, these materials tend to be less chemically stable compared to TiO_2. Additionally, a crystalline compact TiO_2 ETL is compatible with the use of a mesoporous TiO_2 scaffold, shown to improve charge collection, performance, and stability in small and large scale mesoscopic PSC devices [9]. A variety of methods have been developed to produce TiO_2 ETLs with controlled properties of thickness and minimum pin hole density. Spin coating [23,24] and spray pyrolysis [25] are the most widely spread methods in research laboratories due to their ease of application in atmospheric conditions; they can be used to prepare high quality TiO_2 ETLs with thickness ranging between ~ 10-150 nm and very high and conformal surface coverage. More advanced techniques such as e-beam processing [26], low temperature sputtering [27], atomic layer deposition (ALD) [14,28], or anodization [29] are less used but have been shown to produce quality TiO_2 ETLs; for each technique optimal device performance were demonstrated on 2-10 nm/ALD, 40 nm/low-T sputtering, 45-60 nm/e-beam, and 40 nm/anodization ETLs.

The role of the ETL in PSCs is two-fold: it conveys electrons from the perovskite layer to the anodic substrate, acting as a dipole, whilst preventing performance loss related to shunting, e.g. electron-hole recombination at that the perovskite/anode interface. The influence of the ETL's properties on device performance have been well described in devices tested under 1 sun [22,30–32] but very little emphasis has been given on the increased importance of the ETL in low light conditions. Di Giacomo *et al.* [33] showed that a TiO_2 ETL prepared by atomic layer deposition, basically pin-hole free, enabled much higher device performance under 200 lux illumination compared to ETLs prepared by spin coating or spray pyrolysis, despite all devices showing similar outputs under 1 sun. Similar observations were reported for devices tested under 1 sun illumination [25,34]. A number of theories have been advanced to explain hysteresis in perovskite solar cells which are still a cause for debate: ion migrations [35,36], charge separation at interfaces [37,38], charge trapping and de-trapping [39],

ferroelectric polarization [40], and capacitive charging [41]. These topics have now been widely studied under 1 sun illumination, but again, very little importance has been given to the amplitude of hysteresis in devices test under low light illumination. With the attractive prospect of PSCs as indoor power generating technologies which offer a market less accessible to Si-PV, it is increasingly important to understand how parameters affecting device performance and hysteresis under 1 sun translate under low light conditions.

With this work, we aimed to systematically investigate the influence of a TiO_2 compact ETL on device performance and hysteresis under 200 lux (fluorescent lamp) compared to 1 sun (xenon lamp) illumination. We purposely chose to build our devices based on the classic FTO/TiO_2/CH_3NH_3PbI/Spiro-OMeTaD planar architecture to emphasize the impact of ETL structural defects at the ETL/perovskite interface. Whilst this type of devices are known to generate limited outputs, usually between 8-12 % average PCEs with champion cells reaching up to ~15 % [23,24,27,42], their simplicity is of great interest to those focusing their research efforts in understanding the impact of manufacturing process parameters and the development of industry-compatible fabrication methods. Here, the ETLs were prepared by spray pyrolysis of a Ti-organo precursor with the application of 0-50 sprays. We first present a thorough investigation of the structural properties of the ETLs, with particular emphasis of the thickness and pinhole density. The thickness and conformal character of the blocking layers are revealed by top-view and cross-section electron imaging observations. The pinhole density is semi-quantitatively assessed by x-ray photoelectron spectroscopy (XPS) over small areas (~ 0.2 mm^2) and controlled over much larger areas (~ 1 cm^2) by cyclic voltammetry (CV). Semiconductor properties of the c-TiO_2 layers are compared in terms of lateral resistance by transfer length measurements (TLM). Emphasis is given on using adequate characterisation methods: for instance, we show that the crystallinity of sprayed c-TiO_2 layers, initially investigated by grazing angle x-ray diffraction (XRD), is better and faster resolved using Raman spectroscopy. In the second part of this work, planar PSC device performance and hysteresis behaviour are examined and discussed based on I/V data collected at 1 sun and 200 lux and open circuit (V_{oc}) decay measurements. We correlate and compare levels of ETL defects such as pinhole density and excessive film thickness to device performance and hysteresis under both lighting conditions. Finally, we highlight the incresingly detrimental impact of these defects on low light device parameters.

Experimental

Fabrication of TiO_2 layers

Fluorine-doped tin oxide (FTO) glass substrates (Solaronix TCO22-7, TEC7) were cleaned in an ultrasonic bath by dipping in solutions of Hellmanex III detergent (Hellma Analytics), acetone, and isopropanol sequentially for 10 minutes; the substrates were dried using compressed nitrogen between each step. Cleaned substrates were finally subjected to 15 minutes of UV-ozone plasma treatment.

The deposition of the ETLs was performed using atmospheric spray pyrolysis: the spray system comprised of a simple handheld spray gun (Draper 07230) connected to compressed dry air at 25 psi as the carrier gas. For the TiO_2 precursor, titanium diisopropoxide bis(acetylacetonate) (Ti-AcAc, 75 wt.% in isopropanol, Sigma Aldrich) was mixed with isopropanol in a ratio of 1:9 v/v. Clean substrates were heated to 350 °C on a hotplate before a series of sprays were applied using the spray system, at a rate of 5 mL per 25 sprays dispensed over a 10x10 cm^2 glass substrate. One pass was typically 2 seconds long allowing around 15 seconds between each spray cycle for solvent evaporation and the substrate to return to target temperature. After spray deposition, the heated substrates were transferred to an oven and calcined in air for 45 minutes at 500 °C.

Characterisation of TiO_2 layers

Structural properties (thickness, coverage yield, conformity) of the ETLs were investigated by combining electronic imaging, X-ray Photoelectron Spectroscopy (XPS), and cyclic voltammetry analyses. The ETLs were observed by top-down secondary electron imaging using a Hitachi S4800 FEG-SEM (5 kV, WD 8 mm). Cross sections were prepared after a standard scribe fracture using a Hitachi IM4000 Plus Ar broad beam ion miller with a probe current of 4 kV for 1.5 hours. Samples were mounted onto a conductive holder and coated in 5 nm Pt to avoid charging effects and analysed using 10 kV, 10 mA beam parameters at 4-5 mm working distance. XPS data were collected using a Kratos Axis Supra instrument equipped with a monochromated Al Kα X-ray source (225 W) and integral charge neutraliser: points were recorded with 0.1 eV step size, 250 ms dwell time and a pass energy of 20 eV. Calibration was performed against the adventitious carbon peak at 284.8 eV and the data quantified using Shirley backgrounds in CasaXPS 2.3.17dev6.4k. The ETLs were also subjected to cyclic voltammetry (50 $mV.s^{-1}$) in a solution of 0.5 mM $K_4Fe(CN)_6$ + 0.5 mM $K_3Fe(CN)_6$ in aqueous 0.5 M KCl at pH 4 against a KCl saturated Hg_2Cl_2/Hg calomel reference electrode.

Crystalline properties of the ETLs were first assessed by X-Ray Diffraction (XRD) analysis, using a D8 Discover instrument from Bruker Ltd (Cu source at 40 mA & 40 kV). Different analytical settings were tried: scans were run in standard powder diffraction mode at 1.5° 2θ/min (0.050° 2θ angular resolution, 2s per step) followed by grazing angle measurements at 0.12° 2θ/min (0.004° 2θ angular resolution, 2s per step)with incident beam at 2° in 2θ. Following this, the crystalline and semiconductor properties of the ETLs were assessed by Raman micro-spectroscopy and resistive measurements. Raman data were acquired using a Renishaw inVia confocal Raman, 532 nm laser excitation, 1800 gr/mm grating over a shift range of 70 $cm^{-1} \leq \Delta\lambda \leq 700\ cm^{-1}$. Transfer length measurements were performed using a Keithley 2400 sourcemeter attached to cantilever probes on 100 mm x 15 mm substrates. Gold contact bars (2 mm x 15 mm) were evaporated onto ETL/FTO samples with incremental gaps ranging from 1 mm to 7 mm.

Device fabrication

Glass substrates (Solaronix TCO22-7, TEC7) with dimensions 2.4 cm x 2.4 cm were masked with an electrode pattern to create counter electrode contact areas and etched using zinc powder with 2M hydrochloric acid. Substrates were cleaned and TiO_2 ETLs deposited according to the procedure

described above. Lead iodide (PbI_2, 99%, Sigma-Aldrich) and methylammonium iodide (CH_3NH_3I, MAI, 98%, Dyesol) were used as purchased. A precursor solution of 1.45 M MAI and equimolar PbI_2 was prepared in a 4:1 mixture of Dimethylformamide (DMF) and dimethyl sulfoxide (DMSO). The solution was spun onto the prepared substrates at 4000 rpm for 30 s in ambient conditions (20 °C, 65%RH). Instant-crystallisation of the perovskite was accomplished by dripping ethyl acetate (EA) onto the spinning substrate 10 seconds before the spinning process finished. The films were immediately heated at 100 °C for 10 mins to allow for the evaporation of any residual solvent. Substrates were transferred to a nitrogen glovebox and a Spiro-OMeTAD hole transport solution was spun on at 2000 rpm for 45s. This solution was prepared by dissolving 75 mg of 2,2',7,7'-Tetrakis[N,N-di(4-methoxyphenyl)amino] -9,9'-spirobifluorene (Ossila, Spiro-OMeTAD), 30 µl of 4-tert-butylpyridine and 520 mg ml^{-1} $LiN(CF_3SO_2)_2N$ in 1 ml of chlorobenzene. Devices were stored overnight in a low humidity box. Au contacts (100 nm) were thermally evaporated onto the substrates to complete the devices.

MAPI films and devices were also prepared using the toluene drop casting method developed by Jeon *et al.* [43] This anti-solvent method used to be applied as standard in our laboratories until it was found that the ethyl acetate-based method developed by Yin *et al.* [44] provided MAPI layers with much larger coverage yield and lower roughness [45], both critical parameters to this study. In the case of toluene based method, the films were prepared using the same MAPI precursor, which was spun in the ambient conditions described above for 50 s at 4000 rpm and the toluene was dropped 25s before the end of the cycle.

Device characterisation

Active areas of devices were masked (0.1 cm^2 aperture) before testing under a Class AAA solar simulator at AM 1.5G (100 mW cm^{-2}) (Oriel Sol3A) calibrated with a KG5 IR-filtered silicon cell (Newport Oriel 91150-KG5). A total number of 48 pixels were tested: 8 pixels per cell with 6 different types of cells. Low light measurements were conducted using the same mask under an array of compact fluorescent light (CFL) bulbs at 200 lx, calibrated with a Thorlabs S401C thermal sensor. Current density - voltage (J-V) measurements were collected using a Keithley 2400 sourcemeter at a scan rate of 0.1 $V.s^{-1}$, allowing the detection of hysteresis phenomena. Photovoltage decay measurements were performed using a home-built setup. Illumination was provided by a white LED (Bridgelux) giving approximately 1 sun equivalent intensity. Cells were illuminated long enough for the open-circuit voltage to reach a steady state (~1 minute). Voltages were recorded via the analog input of a National Instruments USB-6251 data acquisition board using Wavemetrics IGOR Pro software. The software also controlled the LED switching.

Results & Discussion

1) Properties of TiO_2 layers produced by spray pyrolysis of a TiAcAc precursor

a) Thickness and pin-hole density

In this section, structural properties of TiO_2 layers prepared by application of 0-50 sprays of a Ti-AcAc precursor are investigated. SEM observations and XPS data are combined to determine how the iterative application of sprays of Ti-precursor relates to the thickness and pinhole density of material deposited. High resolution SEM images of TiO_2 layers prepared using 1, 5, 25 and 50 sprays of the Ti-precursor are presented in Figure 1. These demonstrate that with the application of 5 sprays and over, films produced appear to cover most the FTO surface, in the form of a conformal coverage, e.g. with very little variation in thickness. The application of a single spray was found to form very thin and scattered visible at the top of FTO crystals, as per highlighted in Figure 1. With the application of 5 sprays gaps were filled and the build-up of a conformal, yet very thin layer of TiO_2, was revealed by the rounded aspect of FTO crystals. In 25 and 50 spray samples, the excessive thickness of sprayed layers lead to the initiation of very thin cracks especially over the edge of FTO crystals where higher tension forces are exerted on the films. These are often reported in sintered TiO_2 films and tend to be caused by mechanical stresses induced upon cooling [46]. The density of cracks appeared to be more pronounced in the 50-spray sample. Although this could not be confirmed with these images, it is possible the cracks may propagate all the way through to the FTO substrate, generating very small pinholes such as reported by Kavan *et al*. [47] Accumulation of Ti-AcAc precursor in places were found to crystallise into small TiO_2 particles of approximately 20 nm in size (Figure 1, 50 sprays-insert) layer. These small crystals also formed within the thick layer of deposited material, providing the latter with a rougher surface finish (compared to the 15 sprays sample) which is evidenced by comparing the cross-sectional images of the 15 and 50 spray samples.

The thickness of 0-50 spray layers was initially investigated using white light interferometry mapping (SI Figure 1). However, these measurements proved extremely challenging owing to the combined transparency and roughness of the FTO substrate. Instead, cross-sectional SEM imaging was performed on ion beam milled 15-50 sprays samples (Figure 1: CS images of 15 and 50 sprays samples), demonstrating an increase in thickness from approximately 20 nm to 60 nm. This suggests a linear build-up in thickness of about 1.2-1.3 nm/spray. In previous work [48], we suggested a higher build-up of 2 nm layer of TiO_2 per spray but the Ti-organo precursor was prepared in ethanol as opposed to isopropanol, leading to the formation of rougher materials deposits. Similar observations were reported by Jiang *et al.* [49] who studied the impact of solvent wetting and boiling point properties on the structure of TiO_2 layers prepared by spray pyrolysis.

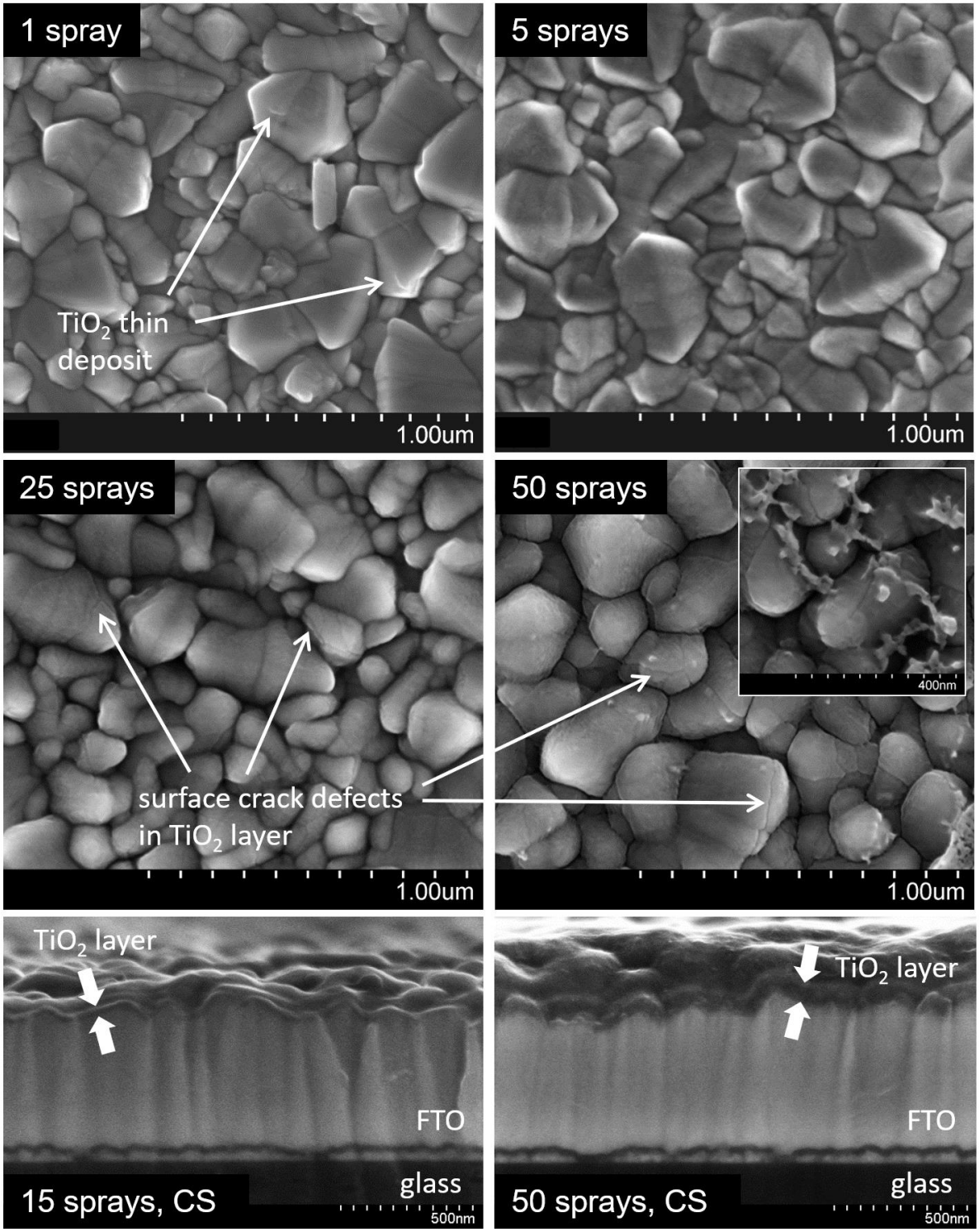

Figure 1. Top-view (top 4 images) and cross-sectional (CS, bottom 2 images) electron microscopy images of TiO_2 ETLs prepared by application of 0-50 sprays of a Ti-AcAc (10 vol.%)/IPA (90 vol. %) precursor on top of TEC7 FTO-coated glass.

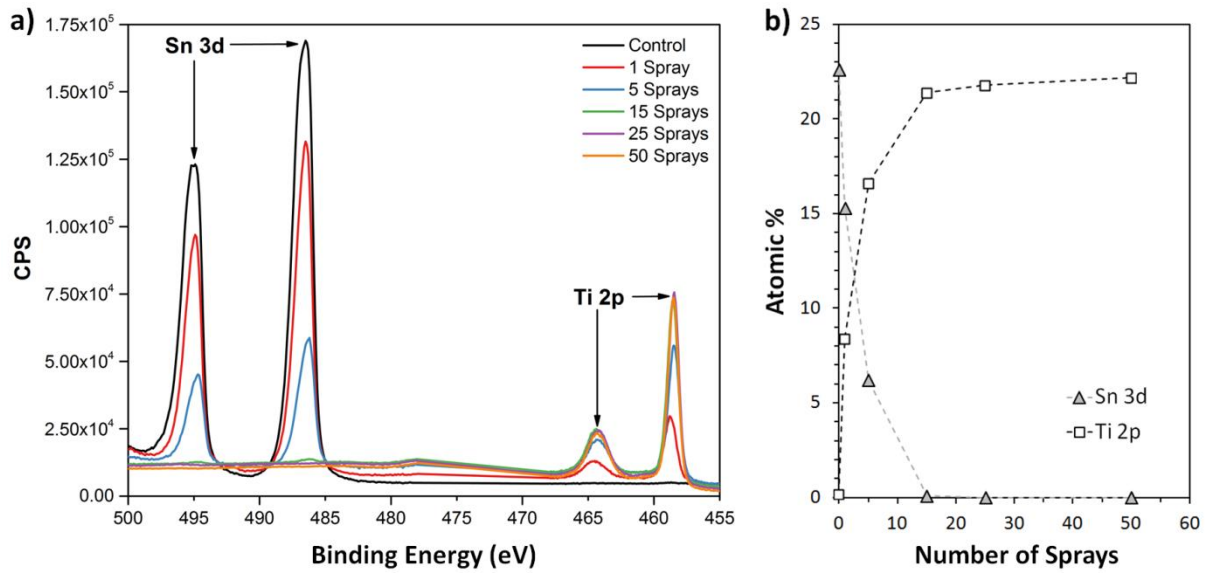

Figure 2. Qualitative (left) and quantitative (right) XPS analyses of TiO_2 ETLs (0-50 sprays).

The coverage yield of 0-50 spray TiO_2 ETLs was assessed over small sample areas of 300*700 μm^2 by XPS and ~ 1 cm^2 by cyclic voltammetry. XPS data collected between 455-500 eV binding energy (Figure 2a) confirmed the presence of titanium and tin with peaks at 486.5 eV and 495.1 eV assigned to Sn $3d_{5/2}$ and $3d_{3/2}$ and peaks generated by the surface of the FTO substrate and peaks at 458.5 eV and 464.5 eV assigned to Ti $2p_{3/2}$ and $2p_{1/2}$ generated by the TiO_2 layer. Quantitative analysis of these data are represented against the number of sprays applied in Figure 2b (quantitative XPS data of all elements are provided in SI Table 1). Figure 2b shows a rapid increase of the Ti at% as the number of sprays increases. XPS is a surface sensitive technique, with the analysis depth limited to < 10 nm by the inelastic mean free path of the measured photoelectrons escaping from the substrate over the energy range of interest [50]. Hence the observed increase in Ti at% is attributed to the thickening and improved coverage of the ETL. An almost symmetrical inverse trend is observed for Sn with only 0.1 at.% at 15 sprays and a complete loss of signal for samples which received ≥ 25 sprays. This complete loss of the underlying Sn signal is taken to indicate that: 1) the average thickness of the overlying ETL film exceeds 10 nm over the whole XPS analysis area, 2) any cracks (Figure 1), defects or pinholes are superficial and still allow > 10 nm ETL thickness within the analysis area. Tin and titanium oxides have very similar atomic densities: 2.78 at/cm^3 for SnO_2 cassiterite vs. 2.86 at/cm^3 for TiO_2 anatase. If we assume that most of XPS counts are generated by electrons escaping from the top 10 Å [51] of the FTO/ETL samples, and that a single spray of Ti-AcAc generates ~ 1.2 nm thick isolated deposits (based on Figure 1), we can approximate the density of pinholes, $x_{pinholes}$ (unit: cm^2 of bare FTO/cm^2 of substrate), as per expressed in Equation 1:

$$x_{pinholes} \sim \frac{at.\%_{Sn}}{(at.\%_{Ti} + at.\%_{Sn})} \qquad \text{Equation 1}$$

This equation was applied for all samples and corresponding pinhole surface densities reported in SI table 1. According to these calculations the applications of 0, 1, 5, and 15 sprays produced TiO_2 layers with 0, 35.4, 62.8, and 99.5 % coverage yield. These calculations are overall in good agreement with electron microscope observations, except maybe for the case of a 5 spray TiO_2 layer. Whilst SEM top view images showed a quasi-complete coverage yield, XPS quantitative data suggest as high as 37.2% pinhole density. This discrepancy was elucidated by electrochemical characterisation of the TiO_2 layers over large sample areas.

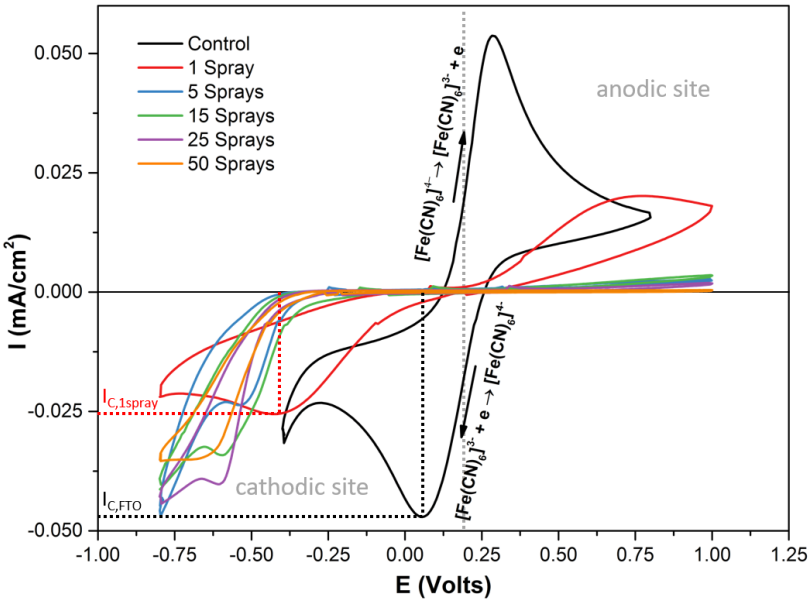

Figure 3. Cyclic voltammetry measurements performed at the surface of FTO glass samples covered with 0-50 spray ETLs ($Fe(CN)_6^{3-/4-}$ electro-couple, pH 4).

To complete this part of our study we applied an analytical method developed by Kavan *et al.* [47] where cyclic voltammetry is used to electrochemically assess the presence of pinholes in TiO_2 blocking layers. This method was also adopted by Su *et al.* [52] to quantify the coverage of TiO_2 layer electrodeposited on FTO substrates. They used the ratio of cathodic peak current of TiO_2/FTO samples vs. FTO to quantify the pinhole surface fraction. These combined methods were applied here to assess the pinhole density of 0-50 spray TiO_2 layers over ~ 1 cm^2 areas (almost 500 x the XPS analytical area). A $Fe(CN)_6^{3-/4-}$ redox couple was chosen as an analyte which small size of ~ 4.3 Å was well suited to detect pinholes through narrow TiO_2 cavities and capillaries. Figure 3 shows the cyclic voltammetric profiles collected at 50 mV/s in 0.5 M KCl for 0-50 spray samples. The control sample (FTO) displayed a cyclic profile typical of the reversible oxidation (top right) and reduction (bottom left) of the $Fe(CN)_6^{3-/4-}$ couple, proceeding with very little resistance. This behaviour was greatly affected by the deposition of 1-50 spray TiO_2 layers with a significant reduction of the cathodic current. Even a single spray TiO_2 layer was found to slow down the oxidation and reduction of $Fe(CN)_6^{3-/4-}$; the broadening of the cathodic peak is indicative of the slow transport of an important fraction of electrons through the TiO_2 deposits. For this sample, a ratio $I_{C,1spray}/I_{C,FTO}$ of ~ 0.541 suggests 54.1% pinhole surface fraction. This is a bit less than the 64.6% estimated by XPS analysis. It is possible that coverage yields calculated based on XPS quantitative data were slightly overestimated due to Sn 3d counts generated by areas of FTO covered with less < 1nm thick TiO_2 deposits. Also, the XPS coverage may differ randomly from the CV coverage because it only surveys a very small sample area compared to CV. This difference emphasizes the importance of controlling materials deposition and properties over large areas, representative of active PV module cell dimensions. With the application of 5 sprays and over, TiO_2 layers display increasingly pronounced blocking effects identified by a very slow increase of the cathodic current far below the standard potential of $Fe(CN)_6^{3-/4-}$ (vs. Hg/Hg_2Cl_2). For these samples the cathodic current loops measured between -0.28 mV and -0.85 mV actually relate to electrochemical phenomena involving the electrolyte rather than the reduction of $Fe(CN)_6^{4-}$. Hence, it is difficult to quantify accurately the coverage of the TiO_2 layer for these samples based on the $I_{C,5\text{-}50pray}/I_{C,FTO}$ ratio. But it can be assumed that with a ratio $I_{C,5\text{-}50\ sprays}/I_{C,FTO} < 10$ (at a potential of $V_{C,1\ spray}$ ~ -0.35 V), pinholes represent less than 10 % in 5-50 spray TiO_2 layers, in agreement with SEM observations (Figure 1). This part of the study confirms that pinhole surface densities estimated based on quantitative XPS data can be overestimated. All combined, high magnification SEM observations, XPS characterisation, and cyclic voltammetry measurements of 1-50 sprays TiO_2 layers demonstrate that a minimum number of 15 sprays must be applied to produce a complete coverage of the FTO-glass substrates over areas of

dimensions representative of cells designed for the fabrication of modules [7,11]. To summarise observations made by SEM, analysis of XPS and cyclic voltammetry data, a schematic representation of structural features of 0-50 sprays TiO_2 layers is proposed in Figure 4.

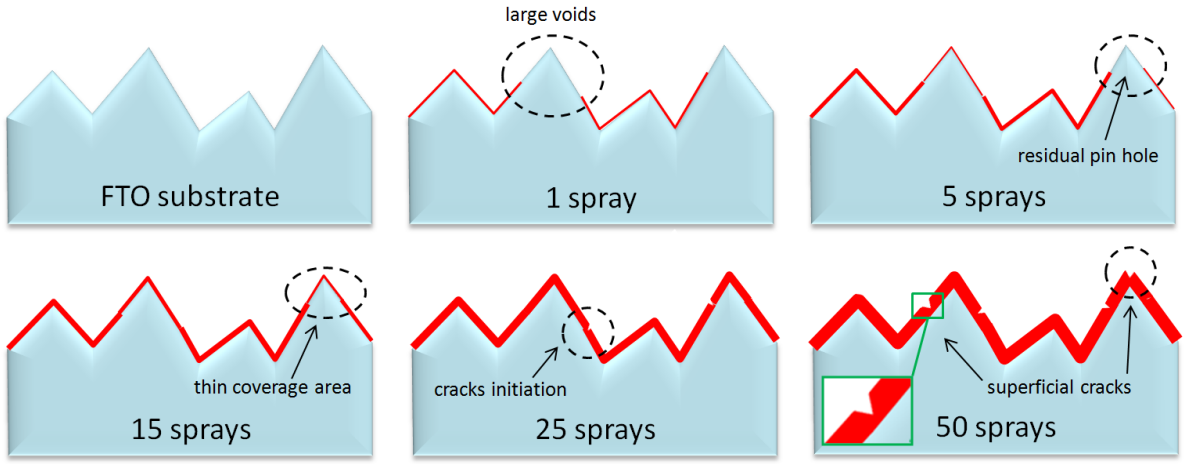

Figure 4. Schematic of the structural properties of TiO_2 ETLs prepared by application of 0-50 sprays of a Ti-AcAc (10 vol.%)/IPA (90 vol. %) precursor followed by sintering at 500 °C for 30 mins.

b) Crystalline and resistive properties of compact TiO_2 layers

Recent publications have suggested that the crystallinity TiO_2 compact layers isn't critical to the fabrication of high efficiency planar PSCs. For instance, Qiu *et al.* [26] produced working devices with efficiences up to 14.6 %. These were built on 15-80 nm TiO_2 layers prepared by electron beam evaporation of TiO_2 pellets. Their XRD data doesn't show any trace of crystalline anatase TiO_2 and the authors conclude from the absence of the (101) peak at 25.3° that their TiO_2 layer is fully amorphous. Unfortunately no scan parameters or instrument settings (angular resolution, speed, grazing angle, etc) were provided; we feel this makes the interpretation of the data questionable. Another study by Huang *et al.* [53] reports 13-15 % planar devices built on ~ 30 nm sputtered TiO_2 layers. The authors explain that increased levels of crystallinity (TiO_2 anatase) resulted in improved electron transport properties, increased J_{sc}, and overall device performance. But they also claim that amorphous TiO_2 can be used to make devices with PCEs averaging 13.30 %. The assessment of the crystalline properties of the films, in our opinion has been overlooked: 1) the XRD instrument settings (5° in 2θ/mins, 40kV, 40 mA) are in our experience inadequate to conclude on the crystalline character of 30 nmTiO_2 layers, let alone quantifying crystalline/amorphous contents; 2) provided the TiO_2 layers produced in that work are textured and have preferential (101) orientation, single SAED analysis may not be conclusive of their crystallinity. Finally, Di Giacomo *et al.* reported working small to large scale flexible devices prepared on an 11 nm ALD amorphous TiO_2 blocking layer [9]. In this case, mesoscopic architecture devices exhibited much higher performance compared to planar control devices. The authors explain that the ALD TiO_2 layer provided good hole blocking properties but considerably slowed down electron transport, hence the low PCEs (~ 1%) of planar devices. Following this short review, we believe there is not enough convincing evidence yet to demonstrate the successful fabrication of high performance planar PSCs on a fully amorphous TiO_2 compact layer.

In this part of our study, we demonstrate the limitations of classic powder XRD analysis in assessing the crystalline properties of very thin TiO_2 ETLs and suggest an alternative method based on the use of Raman spectroscopy. A 50 spray ETL (~ 50 nm) was subjected to various XRD analytical settings. First, a regular XRD powder mode was applied with scan speed of 1.5° 2θ/min, which is 3 times slower compared to scans reported by Huang *et al*. [53]. Figure 5a shows that data collected in classic powder mode did not resolve the anatase (101) peak expected at ≃ 25.3° (2θ). This is despite

applying a 500 °C heat treatment over 30mins which is expected to convert of all amorphous TiO_2 material into crystalline TiO_2 anatase. To resolve the anatase (101) peak, it was necessary to slow down considerably the angular scan speed of data acquisition to 0.120° 2θ/s and use grazing incidence analytical settings. With this settings the acquisition of the full TiO_2 XRD scan (20-80° 2θ) necessary to compute phase quantification would have to run over 500 mins. The optimum incident beam angle, e.g. providing the best signal to noise ratio and peak separation, was found at 2° in 2θ. The same approach was adopted to characterise thinner layers (1-25 sprays). Despite our best efforts to optimise the incident angle, the (101) TiO_2 anatase proved extremely delicate to resolve.

To circumvent these analytical difficulties, Raman spectroscopy, a fast and surface sensitive technique was applied to 0-50 spray ETLs (1.2 µm diameter spot areas). The data collected is reported in Figure 5b which shows peaks at 144 cm^{-1} and 636 cm^{-1}, 394 cm^{-1}, and 516 cm^{-1}, characteristic of vibrational mode E_G, B_{1G} and A_{1G} vibration modes of crystalline TiO_2 anatase [54]. Other small peaks identified by star symbols were generated by the substrate and assigned to vibration modes of SnO and SnO_2 present in FTO [55]. Data collected from a 50 spray ETLs confirmed the crystalline character of TiO_2 layers prepared by spray pyrolysis of a Ti-AcAc precursor followed by high temperature (500 °C) sintering. This is true of all other ETLs prepared in this work. However, for samples prepared with fewer than 15 sprays (< 20 nm), there wasn't enough material to generate a detectable Raman signal, even at 144 cm^{-1} where the dominant E_G peak is expected. In the 5 spray ETL sample, the presence of material at the surface of FTO could be deduced from the attenuation of the FTO peak at 562 cm^{-1}. But a 1 spray ETL/FTO sample produced exactly the same trace as the control sample of bare FTO. To conclude, we showed here that all layers produced in this work contained large amounts of crystalline TiO_2 anatase, although characterised with a very short crystalline range. We also demonstrated Raman spectroscopy to provide a much faster (30s scans) and more reliable analytical route to qualitatively assess the crystalline properties of thin (≥ 15 nm) TiO_2 layers, compared to XRD analysis. Enabling large scale manufacturing of perovskite photovoltaics will require the development of quality control protocols that can guarantee the production of PV modules will consistent outputs and stability. There we believe Raman spectroscopy may be implemented to systematically assess crystalline properties of very thin (> 10 nm thickness) semiconductor films. In the case of TiO_2 ETLs, samples of known crystalline composition may be used to build a calibration curve based on the intensity of the Eg (144 cm^{-1}) TiO_2 anatase peak; matched against Raman data collected from quality control samples selected off the production line would inform manufacturers of any flows or changes in the process.

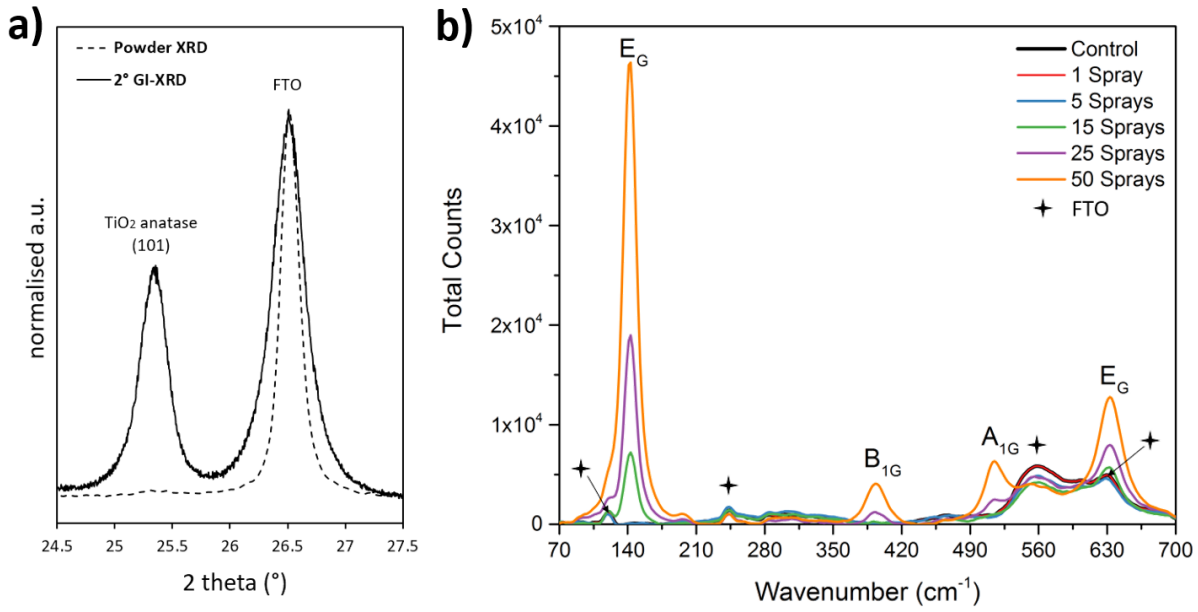

Figure 5. (a) XRD data collected on a 50 spray TiO_2/FTO sample using classic powder x-ray diffraction and (2°) grazing incidence; and (b) Raman spectra of 0-50 sprays TiO_2 ETL/FTO samples.

Semiconductor properties of 0-50 spray TiO_2/FTO samples were investigated using resistance transfer length measurement (TLM), reported in Figure 6a. With this, we aimed to correlate the thickness of TiO_2 layers with current resistive losses in lateral charge transport. Samples were prepared as described in the experimental section with gold contacts evaporated on top of the TiO_2 layer at incremental distances ranging from 1 to 7 mm (Figure 6b). All samples displayed a linear increase in resistance against contact separation, a confirmation that lateral electron transport is affected by the resistive properties of TiO_2/FTO. The slope of these linear trends was also found to increase with the number of sprays applied. For instance, the resistance of a 50 spray TiO_2/FTO bi-layer across increasingly distant contacts rises approximately 7 times faster than in the case of a control FTO sample. The reduced mobility of charges through the TiO_2 layer compared to FTO is also evidenced by the increased resistance measured at a specific contact distance across the range of TiO_2 layer thickness. For instance at 1 mm separation, the resistance of a 50 spray TiO_2/FTO sample (~ 30.5 Ω) is over 10 times higher than the resistance of a 1 spray TiO_2/FTO sample (~ 3.2 Ω). We noticed that the resistance profile collected over the 1 spray TiO_2/FTO sample was almost identical to the control FTO sample. This is in good agreement with our cyclic voltammetry measurements suggesting a low coverage yield of 54.1%. To summarise, this part of our study emphasizes the importance of optimising module designs. Limiting current losses can be achieved by selectively removing the TiO_2 compact layer prior to the printing of metallic current collectors; this has been successfully demonstrated using laser ablation [56]. Patterning the TiO_2 layer by ink jet printing, a technique rapidly becoming compatible with large scale manufacturing of semiconductors, may also provide an attractive alternative in the near future.

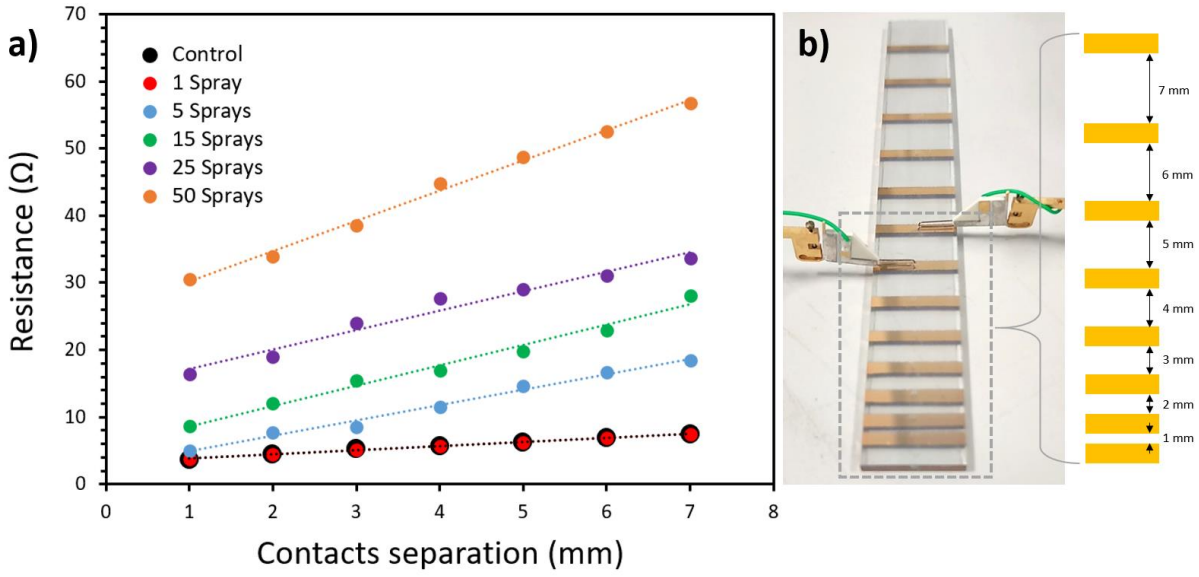

Figure 6: (a) TLM resistance measured across 1-7 mm contact separations for 0-50 spray TiO_2 ETL/FTO samples; (b) picture of the TLM measurements contacts set-up on an TiO_2/FTO sample.

2) Device performance and hysteresis

Planar lead iodide perovskite solar cells (PSCs) were fabricated over 0-50 spray TiO_2 electron transport layers. The coverage yield of the perovskite layer was optimised (details of optimisation study provided in SI section) by using an anti-solvent dripping technique [44]. The photovoltaic performance (η%), open circuit voltage (V_{OC}), current density (J_{SC}), and fill factor (FF) of 48 PSCs (8 pixels per type of cell/ETL) were collected in reverse (V_{oc} to I_{sc}) and forward (I_{sc} to V_{oc}) scanning ($0.1V.s^{-1}$ scan rate) at AM 200 LUX illumination and compared to the traditional 1.5G (1 sun) light testing conditions. All results are reported in Figure 7 and 8, respectively, and typical I/V curves are presented in SI Figure 3.

The efficiency chart produced for devices tested under low light conditions (200 lux, Figure 7) shows optimised outputs for cells built on 25 spray TiO_2 ETLs with an average of 11.7 %, resulting from the optimum combination of J_{sc}, V_{oc}, and Fill Factor. The properties of sprayed ETLs were found to affect all three parameters. For instance, average V_{oc} values double, from 0.34 V to 0.68 V, for devices built on 0 to 50 spray ETLs. At low light, V_{oc} tends to suffer greatly the impact of charge recombination owing to the low density of charge carriers. By improving the coverage yield of TiO_2 ETLs, charge recombination initiated through pinholes at the interface perovskite/FTO are reduced, reflecting the observed V_{oc} increase. Similar observations were made by Di Giacomo *et al.* [57] when comparing the performance of devices built on ALD vs. spin coated TiO_2 ETLs. Open circuit voltage decay data presented in SI Figure 4 confirm decreasing levels of recombination (slower potential decay) against incremental applications of sprays. The spread of V_{oc} data critically narrows down for devices built on 15-50 sprays ETL, indicative of the improving coverage yield. J_{sc} data also increase for devices built on 0-15 sprays ETLs (from 0.012 $\mu A.cm^{-2}$ to 0.016 $\mu A.cm^{-2}$) owing to lower levels of recombination at the TiO_2/perovskite interface. However, beyond 15 sprays, e.g. for > 15 nm thick TiO_2 ETLs, resistive losses caused by excessive material thickness together with the possible the trapping of electrons impact on charge transfer, causing a 12.5% decrease of the J_{sc}, from 0.016 $\mu A.cm^{-2}$ to 0.014 $\mu A.cm^{-2}$. Reverse scan FF data tend improve relatively to the number of sprays applied, from 40.7 % to 64.8 % for devices built on bare FTO and 25 spray ETL samples, respectively. This again may be related to decreasing pinhole densities and associated reduced recombination losses. Hysteresis is noticeable for most devices, with V_{oc} and J_{sc} forward scan data displaying very similar trends compared to reverse V_{oc} and J_{sc} data but generally at a lower magnitudes. According to Cojocaru *et al.* [58], at 200 lux illumination (equivalent to 0.33 mW/cm^2 in the case of a fluorescent lamp), small voltage losses are expected in forward scans collected at a speed of 0.1 $V.s^{-1}$ due to the capacitive behaviour of interfaces in planar PSCs, in agreement with our results. The lower J_{sc} data collected in forward scan may be assigned to defects in the perovskite layer, more precisely trap states present at grain boundaries and the perovskite/TiO_2 interface [59]. Here, the difference between reverse and forward scan data is particularly noticeable in the case of FF values: the gap appears to widen across the set of devices from 0-50 spray ETLs, suggesting a correlation between the thickness of TiO_2 ETL and the amplitude of hysteresis. Based on the findings of Cojocaru *et al.* [58], we suggest here that thicker TiO_2 may contribute towards an enhanced capacitive behaviour of the device causing exacerbated hysteresis.

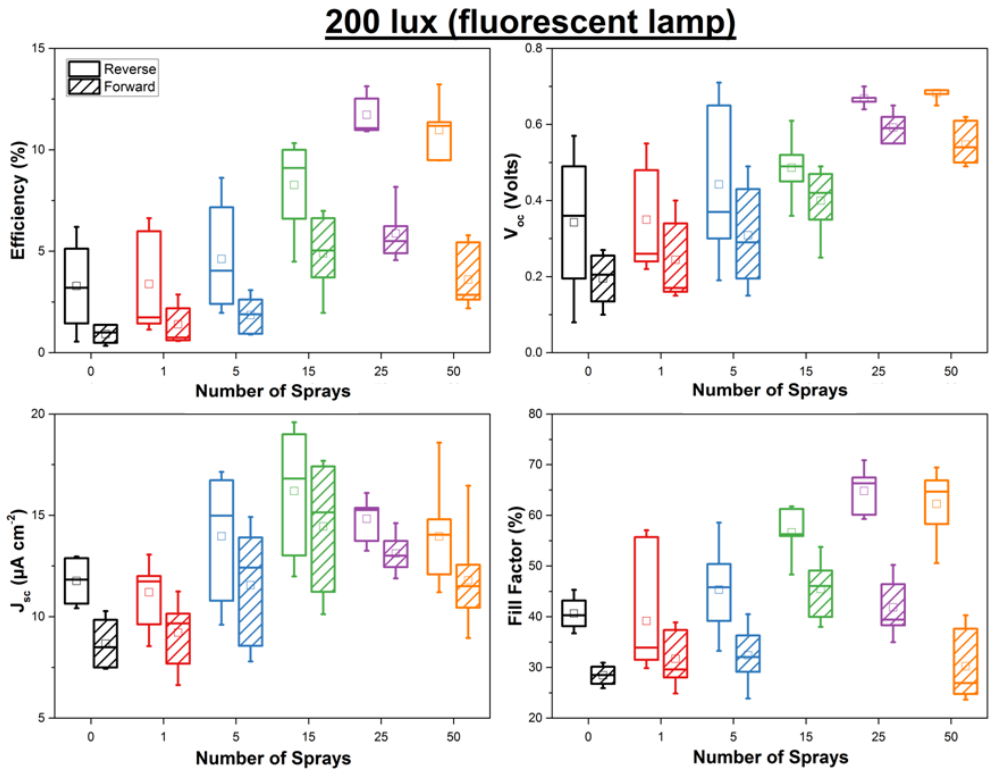

Figure 7. Efficiency, V_{OC}, J_{SC} and fill factor data of PSCs devices built on 0-50 spray TiO_2 ETLs under 200 lux illumination (forward and reverse voltage sweeps).

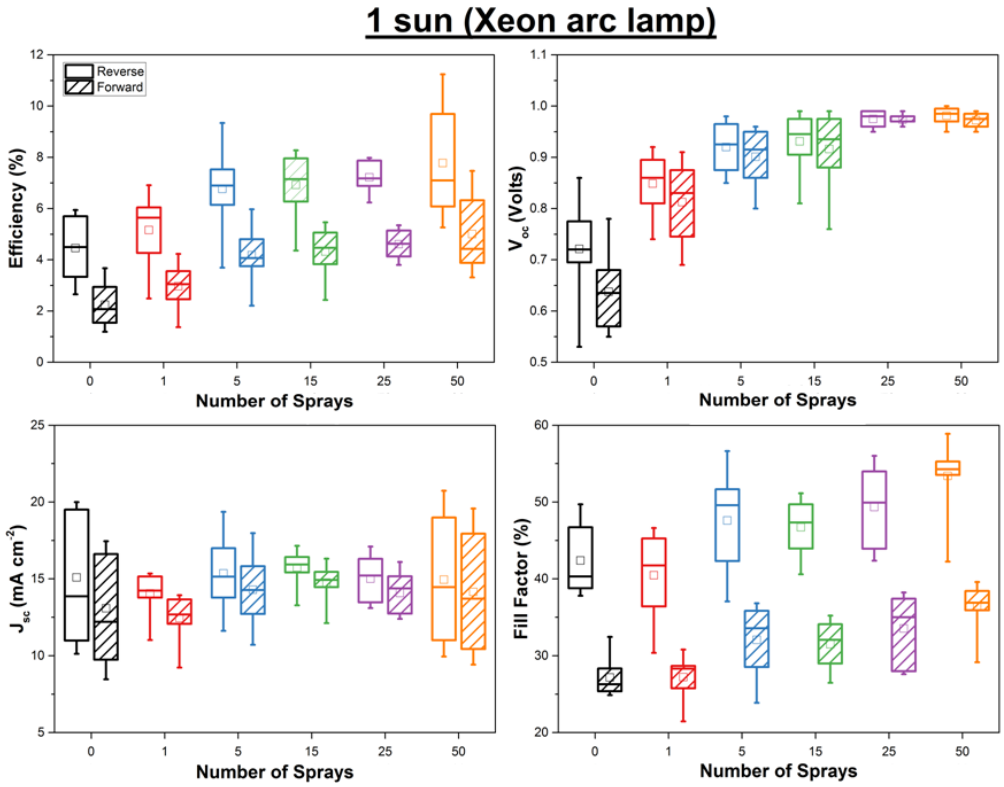

Figure 8. Efficiency, V_{OC}, J_{SC} and fill factor data of PSCs devices built on 0-50 spray TiO_2 ETLs under 1 sun illumination (forward and reverse voltage sweeps).

Data collected under 1 sun illumination (Figure 8) show optimum photovoltaic performance for devices built on 50 spray TiO_2 ETLs, with an average efficiency of 7.7 % in reverse scanning. Device

performance parameters follow similar trends under 1 sun compared to 200 lux. For instance, V_{oc} data increase from 0.72 V to 0.93 V (29.2% increase) for devices built on 0 to 50 spray ETLs; however, this is much less than the progression of V_{oc} from to 0.34 V to 0.68 V (100% increase) recorded under 200 lux illumination. The overall higher V_{oc} data collected under 1 sun reflect a higher density of mobile charges generated, also less susceptible to recombination. J_{sc} values are optimised for devices built on 15 spray ETLs where structural features offer the best compromise between pinhole density and resistive properties in these lighting conditions. The FF data improved with incremental application of TiO_2 precursor. However, the magnitude of hysteresis under 1 sun was found to remain constant regardless of the properties of the TiO_2 ETL. We also observed that differences between reverse and forward J_{sc} and V_{oc} data were lower under 1 sun compared to 200 lux. Overall the amplitude of hysteresis displayed was lower under 1 sun, with 15-20% difference between reverse and forward FF data, compared to 15-30% under 200 lux. These observations suggest that under 1 sun illumination, there are enough charge carriers to overcome defects present in the TiO_2 ETL which impact on hysteresis. However, the consistent gap between reverse and forward FF data reported in Figure 8 suggests that in these lighting conditions hysteresis is related to the perovskite layer and possibly the TiO_2/perovskite interface, for instance ion migrations, which have been suggested a possible cause of hysteresis in PSCs [60,61], The hysteresis phenomena observed here at 200 lux and at 1 sun correlate both scenarios of large-scale trapping of electrons (here in the ETL) and slow ion migrations suggested by Richardson *et al*. [35].

Conclusions

This work systematically investigated the properties of compact TiO_2 layers prepared by spray hydrolysis of a Ti-organo precursor. We found that a minimum of 15 sprays was required for ensuring the fabrication of a pinhole free TiO_2 layer. Through this study, we illustrated the importance of combining small-scale (XPS, SEM) and large scale (cyclic voltammetry) analytical tools to achieve a robust assessment of ETLs properties. We highlighted the importance of applying adequate analytical techniques and protocols, and also recommended the use of Raman spectroscopy over XRD analysis for a rapid and qualitative assessment of crystalline properties of thin TiO_2 semiconductor films.

Planar lead-halide PSCs were built using a classic planar architecture: TiO_2 (0-50 sprays ETLs)/MAPI/Spiro-OMeTAD/Au. This architecture was chosen over a mesoscopic architecture (including a mesoscopic scaffold of TiO_2) to emphasize the impact of the ETL on device performance and minimize the effect of additional parameters induced by the presence of a mesoscopic TiO_2 scaffold (thickness, porosity, etc). However, our main findings apply to some extent to mesoscopic devices which, despite enhanced charge extraction enabled by the large surface area meso-TiO_2/perovskite interface, rely on the presence of a compact ETL to achieve high performance [14]. Optimised devices showed overall much higher performance under 200 lux with an average PCE of 11.7 % for cells built over a 25 sprays ETL compared to 7.8 % under 1 sun for cells built over a 50 sprays ETL. Defects in ETLs such as low coverage and excessive thickness induced up to average PCEs losses of 63 % (200 lux) and 42 % (1 sun) in control devices with no ETL. All devices displayed hysteresis, and importantly, the magnitude of hysteresis was found to critically depend on the properties of the ETL under low light illumination where the capacitive behaviour of TiO_2 increases.

This work highlights the importance of controlling materials deposition to finest degree in the making of lead-halide perovskite solar cells. Whilst spray pyrolysis is a technique available to most research teams to prepare small devices, here we demonstrated that the necessity for a repetitive, time consuming, and high-temperature deposition procedure makes it less recommendable for the fabrication of large scale PSCs. Better device performance have been demonstrated on thinner ~ 2 nm TiO_2 ETLs produced by ALD or e-beam manufacturing, both techniques increasingly used in the industrial manufacturing of semiconductors. Finally, we showed here that optimising the fabrication of PSCs must take into account the end application, namely outdoor vs. indoor PV.

Acknowledgements

This work was supported by the Engineering and Physical Sciences Research Council (EPSRC) through the SPECIFIC Innovation and Knowledge Centre (EP/N020863/1). The XPS, XRD and Raman system were financed by Sêr Cymru Solar, a project funded by the Welsh Assembly Government.

References

[1] A. Kojima, K. Teshima, Y. Shirai, T. Miyasaka, Organometal halide perovskites as visible-light sensitizers for photovoltaic cells, J. Am. Chem. Soc. 131 (2009) 6050–6051. doi:10.1021/ja809598r.

[2] I. Hussain, H.P. Tran, J. Jaksik, J. Moore, N. Islam, M.J. Uddin, Functional materials, device architecture, and flexibility of perovskite solar cell, Emergent Mater. 1 (2018) 133–154. doi:10.1007/s42247-018-0013-1.

[3] NREL, Best Research-Cell Efficiency Chart, (2019). https://www.nrel.gov/pv/cell-efficiency.html (accessed July 18, 2019).
[4] D. Wang, M. Wright, N.K. Elumalai, A. Uddin, Stability of perovskite solar cells, Sol. Energy Mater. Sol. Cells. 147 (2016) 255–275. doi:10.1016/j.solmat.2015.12.025.
[5] L.K. Ono, N.-G. Park, K. Zhu, W. Huang, Y. Qi, Perovskite Solar Cells—Towards Commercialization, ACS Energy Lett. 2 (2017) 1749–1751. doi:10.1021/acsenergylett.7b00517.
[6] N.K. Elumalai, M.A. Mahmud, D. Wang, A. Uddin, Perovskite solar cells: Progress and advancements, Energies. 9 (2016). doi:10.3390/en9110861.
[7] F. De Rossi, J.A. Baker, D. Beynon, K.E.A. Hooper, S.M.P. Meroni, D. Williams, Z. Wei, A. Yasin, C. Charbonneau, E.H. Jewell, T.M. Watson, All Printable Perovskite Solar Modules with 198 cm2 Active Area and Over 6% Efficiency, Adv. Mater. Technol. 3 (2018) 1800156. doi:10.1002/admt.201800156.
[8] H.K.H. Lee, J. Barbé, S.M.P. Meroni, T. Du, C.-T. Lin, A. Pockett, J. Troughton, S.M. Jain, F. De Rossi, J. Baker, M.J. Carnie, M.A. McLachlan, T.M. Watson, J.R. Durrant, W.C. Tsoi, Outstanding Indoor Performance of Perovskite Photovoltaic Cells - Effect of Device Architectures and Interlayers, Sol. RRL. 3 (2019) 1800207. doi:10.1002/solr.201800207.
[9] F. Di Giacomo, V. Zardetto, A. D'Epifanio, S. Pescetelli, F. Matteocci, S. Razza, A. Di Carlo, S. Licoccia, W.M.M. Kessels, M. Creatore, T.M. Brown, Flexible perovskite photovoltaic modules and solar cells based on atomic layer deposited compact layers and UV-irradiated TiO<inf>2</inf> scaffolds on plastic substrates, Adv. Energy Mater. 5 (2015) 1401808. doi:10.1002/aenm.201401808.
[10] T. Sherahilo, Oxford PV sets world record for perovskite solar cell, (2018). https://www.oxfordpv.com/news/oxford-pv-sets-world-record-perovskite-solar-cell (accessed July 16, 2019).
[11] F. Matteocci, L. Cinà, F. Di Giacomo, S. Razza, A.L. Palma, A. Guidobaldi, A. D'Epifanio, S. Licoccia, T.M. Brown, A. Reale, A. Di Carlo, High efficiency photovoltaic module based on mesoscopic organometal halide perovskite, Prog. Photovoltaics Res. Appl. 24 (2016) 436–445. doi:10.1002/pip.2557.
[12] C.Y. Chen, J.H. Chang, K.M. Chiang, H.L. Lin, S.Y. Hsiao, H.W. Lin, Perovskite Photovoltaics for Dim-Light Applications, Adv. Funct. Mater. 25 (2015) 7064–7070. doi:10.1002/adfm.201503448.
[13] J. Dagar, S. Castro-Hermosa, G. Lucarelli, F. Cacialli, T.M. Brown, Highly efficient perovskite solar cells for light harvesting under indoor illumination via solution processed SnO2/MgO composite electron transport layers, Nano Energy. 49 (2018) 290–299. doi:10.1016/j.nanoen.2018.04.027.
[14] A.K. Chandiran, A. Yella, M.T. Mayer, P. Gao, M.K. Nazeeruddin, M. Grätzel, Sub-nanometer conformal TiO_2 blocking layer for high efficiency solid-state perovskite absorber solar cells, Adv. Mater. 26 (2014) 4309–4312. doi:10.1002/adma.201306271.
[15] M. Li, C. Zhao, Z.K. Wang, C.C. Zhang, H.K.H. Lee, A. Pockett, J. Barbé, W.C. Tsoi, Y.G. Yang, M.J. Carnie, X.Y. Gao, W.X. Yang, J.R. Durrant, L.S. Liao, S.M. Jain, Interface Modification by Ionic Liquid: A Promising Candidate for Indoor Light Harvesting and Stability Improvement of Planar Perovskite Solar Cells, Adv. Energy Mater. 8 (2018) 1801509. doi:10.1002/aenm.201801509.
[16] H.K.H. Lee, J. Wu, J. Barbé, S.M. Jain, S. Wood, E.M. Speller, Z. Li, F.A. Castro, J.R. Durrant, W.C. Tsoi, Organic photovoltaic cells-promising indoor light harvesters for self-sustainable electronics, J. Mater. Chem. A. 6 (2018) 5618–5626. doi:10.1039/c7ta10875c.
[17] Y. Cao, Y. Liu, S.M. Zakeeruddin, A. Hagfeldt, M. Grätzel, Direct Contact of Selective Charge Extraction Layers Enables High-Efficiency Molecular Photovoltaics, Joule. 2 (2018) 1108–1117. doi:10.1016/j.joule.2018.03.017.
[18] W. Zhang, J. Xiong, L. Jiang, J. Wang, T. Mei, X. Wang, H. Gu, W.A. Daoud, J. Li, Thermal Stability-Enhanced and High-Efficiency Planar Perovskite Solar Cells with Interface Passivation, ACS Appl. Mater. Interfaces. 9 (2017) 38467–38476. doi:10.1021/acsami.7b10994.
[19] D. Koushik, W.J.H. Verhees, Y. Kuang, S. Veenstra, D. Zhang, M.A. Verheijen, M. Creatore, R.E.I. Schropp, High-efficiency humidity-stable planar perovskite solar cells based on atomic layer architecture, Energy Environ. Sci. 10 (2017) 91–100. doi:10.1039/c6ee02687g.
[20] G. Yang, H. Tao, P. Qin, W. Ke, G. Fang, Recent progress in electron transport layers for efficient perovskite solar cells, J. Mater. Chem. A. 4 (2016) 3970–3990. doi:10.1039/c5ta09011c.

[21] X. Zeng, T. Zhou, C. Leng, Z. Zang, M. Wang, W. Hu, X. Tang, S. Lu, L. Fang, M. Zhou, Performance improvement of perovskite solar cells by employing a CdSe quantum dot/PCBM composite as an electron transport layer, J. Mater. Chem. A. 5 (2017) 17499–17505. doi:10.1039/c7ta00203c.
[22] Y. Hou, C.O.R. Quiroz, S. Scheiner, W. Chen, T. Stubhan, A. Hirsch, M. Halik, C.J. Brabec, Low-temperature and hysteresis-free electron-transporting layers for efficient, regular, and planar structure perovskite solar cells, Adv. Energy Mater. 5 (2015) 1501056. doi:10.1002/aenm.201501056.
[23] G.E. Eperon, V.M. Burlakov, P. Docampo, A. Goriely, H.J. Snaith, Morphological control for high performance, solution-processed planar heterojunction perovskite solar cells, Adv. Funct. Mater. 24 (2014) 151–157. doi:10.1002/adfm.201302090.
[24] B. Conings, L. Baeten, T. Jacobs, R. Dera, J. D'Haen, J. Manca, H.G. Boyen, An easy-to-fabricate low-temperature TiO2 electron collection layer for high efficiency planar heterojunction perovskite solar cells, APL Mater. 2 (2014) 081505. doi:10.1063/1.4890245.
[25] Y. Wu, X. Yang, H. Chen, K. Zhang, C. Qin, J. Liu, W. Peng, A. Islam, E. Bi, F. Ye, M. Yin, P. Zhang, L. Han, Highly compact TiO2 layer for efficient hole-blocking in perovskite solar cells, Appl. Phys. Express. 7 (2014) 052301. doi:10.7567/APEX.7.052301.
[26] W. Qiu, U.W. Paetzold, R. Gehlhaar, V. Smirnov, H.G. Boyen, J.G. Tait, B. Conings, W. Zhang, C.B. Nielsen, I. McCulloch, L. Froyen, P. Heremans, D. Cheyns, An electron beam evaporated TiO2 layer for high efficiency planar perovskite solar cells on flexible polyethylene terephthalate substrates, J. Mater. Chem. A. 3 (2015) 22824–22829. doi:10.1039/c5ta07515g.
[27] A. Alberti, E. Smecca, S. Sanzaro, C. Bongiorno, F. Giannazzo, G. Mannino, A. La Magna, M. Liu, P. Vivo, A. Listorti, E. Calabrò, F. Matteocci, A. Di Carlo, Nanostructured TiO2 Grown by Low-Temperature Reactive Sputtering for Planar Perovskite Solar Cells, ACS Appl. Energy Mater. 2 (2019) 6218–6229. doi:10.1021/acsaem.9b00708.
[28] H. Lu, Y. Ma, B. Gu, W. Tian, L. Li, Identifying the optimum thickness of electron transport layers for highly efficient perovskite planar solar cells, J. Mater. Chem. A. 3 (2015) 16445–16452. doi:10.1039/c5ta03686k.
[29] J. Choi, S. Song, M.T. Hörantner, H.J. Snaith, T. Park, Well-Defined Nanostructured, Single-Crystalline TiO2 Electron Transport Layer for Efficient Planar Perovskite Solar Cells, ACS Nano. 10 (2016) 6029–6036. doi:10.1021/acsnano.6b01575.
[30] J. Tian, H. Li, H. Wang, B. Zheng, Y. Xue, X. Liu, TiO2 composite electron transport layers for planar perovskite solar cells by mixed spray pyrolysis with precursor solution incorporating TiO2 nanoparticles, Chinese Phys. B. 27 (2018) 018810. doi:10.1088/1674-1056/27/1/018810.
[31] J. Liu, G. Wang, K. Luo, X. He, Q. Ye, C. Liao, J. Mei, Understanding the Role of the Electron-Transport Layer in Highly Efficient Planar Perovskite Solar Cells, ChemPhysChem. 18 (2017) 617–625. doi:10.1002/cphc.201601245.
[32] S. Zhang, L. Lei, S. Yang, X. Li, Y. Liu, Q. Gao, X. Gao, Q. Cao, Y. Yu, Influence of TiO 2 Blocking Layer Morphology on Planar Heterojunction Perovskite Solar Cells , Chem. Lett. 45 (2016) 592–594. doi:10.1246/cl.160059.
[33] F. Di Giacomo, V. Zardetto, G. Lucarelli, L. Cinà, A. Di Carlo, M. Creatore, T.M. Brown, Mesoporous perovskite solar cells and the role of nanoscale compact layers for remarkable all-round high efficiency under both indoor and outdoor illumination, Nano Energy. 30 (2016) 460–469. doi:10.1016/j.nanoen.2016.10.030.
[34] V. Zardetto, F. Di Giacomo, G. Lucarelli, W.M.M. Kessels, T.M. Brown, M. Creatore, Plasma-assisted atomic layer deposition of TiO 2 compact layers for flexible mesostructured perovskite solar cells, Sol. Energy. 150 (2017) 447–453. doi:10.1016/j.solener.2017.04.028.
[35] G. Richardson, S.E.J. O'Kane, R.G. Niemann, T.A. Peltola, J.M. Foster, P.J. Cameron, A.B. Walker, Can slow-moving ions explain hysteresis in the current-voltage curves of perovskite solar cells?, Energy Environ. Sci. 9 (2016) 1476–1485. doi:10.1039/c5ee02740c.
[36] Y. Wu, H. Shen, D. Walter, D. Jacobs, T. Duong, J. Peng, L. Jiang, Y.B. Cheng, K. Weber, On the Origin of Hysteresis in Perovskite Solar Cells, Adv. Funct. Mater. 26 (2016) 6807–6813. doi:10.1002/adfm.201602231.
[37] L. Kegelmann, C.M. Wolff, C. Awino, F. Lang, E.L. Unger, L. Korte, T. Dittrich, D. Neher, B. Rech, S. Albrecht, It Takes Two to Tango - Double-Layer Selective Contacts in Perovskite Solar Cells for Improved Device Performance and Reduced Hysteresis, ACS Appl. Mater. Interfaces. 9 (2017) 17245–17255. doi:10.1021/acsami.7b00900.
[38] S.A.L. Weber, I.M. Hermes, S.H. Turren-Cruz, C. Gort, V.W. Bergmann, L. Gilson, A. Hagfeldt, M. Graetzel, W. Tress, R. Berger, How the formation of interfacial charge causes hysteresis in perovskite solar cells, Energy Environ. Sci. 11 (2018) 2404–2413. doi:10.1039/c8ee01447g.

[39] J.W. Lee, S.G. Kim, S.H. Bae, D.K. Lee, O. Lin, Y. Yang, N.G. Park, The Interplay between Trap Density and Hysteresis in Planar Heterojunction Perovskite Solar Cells, Nano Lett. 17 (2017) 4270–4276. doi:10.1021/acs.nanolett.7b01211.
[40] H.S. Kim, S.K. Kim, B.J. Kim, K.S. Shin, M.K. Gupta, H.S. Jung, S.W. Kim, N.G. Park, Ferroelectric polarization in CH<inf>3</inf>NH<inf>3</inf>PbI<inf>3</inf> perovskite, J. Phys. Chem. Lett. 6 (2015) 1729–1735. doi:10.1021/acs.jpclett.5b00695.
[41] O. Almora, I. Zarazua, E. Mas-Marza, I. Mora-Sero, J. Bisquert, G. Garcia-Belmonte, Capacitive dark currents, hysteresis, and electrode polarization in lead halide perovskite solar cells, J. Phys. Chem. Lett. 6 (2015) 1645–1652. doi:10.1021/acs.jpclett.5b00480.
[42] A.K. Chandiran, A. Yella, M.T. Mayer, P. Gao, M.K. Nazeeruddin, M. Grätzel, Sub-nanometer conformal TiO2 blocking layer for high efficiency solid-state perovskite absorber solar cells, Adv. Mater. 26 (2014) 4309–4312. doi:10.1002/adma.201306271.
[43] N.J. Jeon, J.H. Noh, Y.C. Kim, W.S. Yang, S. Ryu, S. Il Seok, Solvent engineering for high-performance inorganic–organic hybrid perovskite solar cells, Nat. Mater. 13 (2014) 897–903. doi:10.1038/nmat4014.
[44] M. Yin, F. Xie, H. Chen, X. Yang, F. Ye, E. Bi, Y. Wu, M. Cai, L. Han, Annealing-free perovskite films by instant crystallization for efficient solar cells, J. Mater. Chem. A. 4 (2016) 8548–8553. doi:10.1039/C6TA02490D.
[45] J. Troughton, K. Hooper, T.M. Watson, Humidity resistant fabrication of CH3NH3PbI3 perovskite solar cells and modules, Nano Energy. 39 (2017) 60–68. doi:10.1016/j.nanoen.2017.06.039.
[46] M. Mahé, J.M. Heintz, J. Rödel, P. Reynders, Cracking of titania nanocrystalline coatings, J. Eur. Ceram. Soc. 28 (2008) 2003–2010. doi:10.1016/j.jeurceramsoc.2008.02.002.
[47] L. Kavan, N. Tétreault, T. Moehl, M. Grätzel, Electrochemical characterization of TiO2 blocking layers for dye-sensitized solar cells, J. Phys. Chem. C. 118 (2014) 16408–16418. doi:10.1021/jp4103614.
[48] C. Charbonneau, P.J. Cameron, A. Pockett, A. Lewis, J.R. Troughton, E. Jewell, D.A. Worsley, T.M. Watson, Solution processing of TiO2 compact layers for 3rd generation photovoltaics, Ceram. Int. 42 (2016) 11989–11997. doi:10.1016/j.ceramint.2016.04.125.
[49] C. Jiang, W.L. Koh, M.Y. Leung, W. Hong, Y. Li, J. Zhang, Influences of alcoholic solvents on spray pyrolysis deposition of TiO 2 blocking layer films for solid-state dye-sensitized solar cells, J. Solid State Chem. 198 (2013) 197–202. doi:10.1016/j.jssc.2012.10.010.
[50] M.P. Seah, W.A. Dench, Quantitative Electron Spectroscopy of Surfaces :, Surf. Interface Anal. 1 (1979) 2–11. doi:10.1002/sia.740010103 .
[51] H.T. Nguyen-Truong, Penn algorithm including damping for calculating the electron inelastic mean free path, J. Phys. Chem. C. 119 (2015) 7883–7887. doi:10.1021/acs.jpcc.5b00403.
[52] T. Sen Su, T.Y. Hsieh, C.Y. Hong, T.C. Wei, Electrodeposited Ultrathin TiO2 Blocking Layers for Efficient Perovskite Solar Cells, Sci. Rep. 5 (2015) 1–8. doi:10.1038/srep16098.
[53] A. Huang, J. Zhu, J. Zheng, Y. Yu, Y. Liu, S. Yang, S. Bao, L. Lei, P. Jin, Room-temperature processible TiO2 electron selective layers with controllable crystallinity for high efficiency perovskite photovoltaics, Sol. Energy Mater. Sol. Cells. 163 (2017) 15–22. doi:10.1016/j.solmat.2017.01.006.
[54] F. Tian, Y. Zhang, J. Zhang, C. Pan, Raman spectroscopy: A new approach to measure the percentage of anatase TiO2 exposed (001) facets, J. Phys. Chem. C. 116 (2012) 7515–7519. doi:10.1021/jp301256h.
[55] C.Y. Kim, D.H. Riu, Raman scattering, electrical and optical properties of fluorine-doped tin oxide thin films with (200) and (301) preferred orientation, Mater. Chem. Phys. 148 (2014) 810–817. doi:10.1016/j.matchemphys.2014.08.055.
[56] A.L. Palma, F. Matteocci, A. Agresti, S. Pescetelli, E. Calabrò, L. Vesce, S. Christiansen, M. Schmidt, A. Di Carlo, Laser-Patterning Engineering for Perovskite Solar Modules with 95% Aperture Ratio, IEEE J. Photovoltaics. 7 (2017) 1674–1680. doi:10.1109/JPHOTOV.2017.2732223.
[57] F. Di Giacomo, V. Zardetto, G. Lucarelli, L. Cinà, A. Di Carlo, M. Creatore, T.M. Brown, Mesoporous perovskite solar cells and the role of nanoscale compact layers for remarkable all-round high efficiency under both indoor and outdoor illumination, Nano Energy. 30 (2016) 460–469. doi:10.1016/j.nanoen.2016.10.030.
[58] L. Cojocaru, S. Uchida, K. Tamaki, P.V.V. Jayaweera, S. Kaneko, J. Nakazaki, T. Kubo, H. Segawa, Determination of unique power conversion efficiency of solar cell showing hysteresis in the I-V curve under various light intensities, Sci. Rep. 7 (2017) 11790. doi:10.1038/s41598-017-10953-3.

[59] Y. Shao, Z. Xiao, C. Bi, Y. Yuan, J. Huang, Origin and elimination of photocurrent hysteresis by fullerene passivation in CH3NH3PbI3 planar heterojunction solar cells, Nat. Commun. 5 (2014) 5784. doi:10.1038/ncomms6784.
[60] A. Pockett, M.J. Carnie, Ionic Influences on Recombination in Perovskite Solar Cells, ACS Energy Lett. 2 (2017) 1683–1689. doi:10.1021/acsenergylett.7b00490.
[61] P. Calado, A.M. Telford, D. Bryant, X. Li, J. Nelson, B.C. O'Regan, P.R.F. Barnes, Evidence for ion migration in hybrid perovskite solar cells with minimal hysteresis, Nat. Commun. 7 (2016) 13831. doi:10.1038/ncomms13831.
[62] A. Pockett, G.E. Eperon, T. Peltola, H.J. Snaith, A. Walker, L.M. Peter, P.J. Cameron, Characterization of planar lead halide perovskite solar cells by impedance spectroscopy, open-circuit photovoltage decay, and intensity-modulated photovoltage/photocurrent spectroscopy, J. Phys. Chem. C. 119 (2015) 3456–3465. doi:10.1021/jp510837q.
[63] R. Gottesman, P. Lopez-Varo, L. Gouda, J.A. Jimenez-Tejada, J. Hu, S. Tirosh, A. Zaban, J. Bisquert, Dynamic Phenomena at Perovskite/Electron-Selective Contact Interface as Interpreted from Photovoltage Decays, Chem. 1 (2016) 776–789. doi:10.1016/j.chempr.2016.10.002.

Electronic Supplementary Information

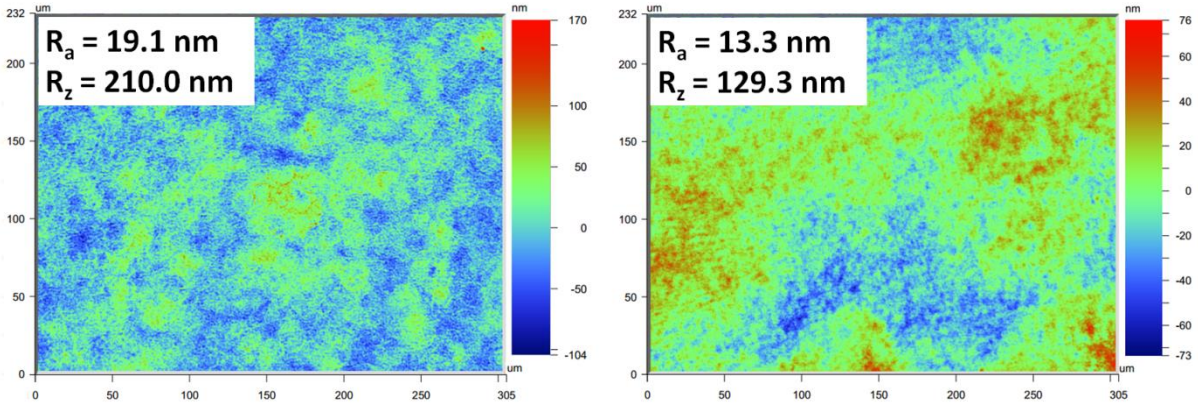

SI Figure 1. White light interferometry repeat measurements of a 50 sprays ETLs deposited prepared on FTO glass substrates.

These images demonstrate the high variability of results obtained with white light measurements, owing to the transparency and high roughness of the FTO substrate.

SI Table 1. Atomic percentages of each elements detected at the surface of 0-50 sprays ETLs and corresponding pinhole surface ratio; these are based on the fitting of XPS data measured over an area of 300*700 µm².

XPS peak	Atomic %					
	0 spray (FTO)	1 spray	5 sprays	15 sprays	25 sprays	50 sprays
O 1s	47.8	48.3	49.7	52.5	52.6	49.6
Sn $3d_{3/2}$	9.3	6.2	2.5	0.0	0.0	-
Sn $3d_{5/2}$	13.3	9.1	3.7	0.1	-	-
Ti 2p	0.2	8.4	16.6	21.4	21.8	22.2
N 1s	0.1	0.4	0.5	0.8	0.5	0.7
Ca 2p	0.1	0.1	0.1	-	-	-
Si 2p	1.3	1.7	1.6	1.8	1.4	0.8
C 1s	26.3	25.3	25.0	23.4	23.1	26.7
K 2p	1.5	0.3	0.5	-	0.6	-
F 1s	0.1	0.1	-	-	-	-
$x_{pinholes}$ (%)	99.2	64.6	27.2	0.5	0	0

Optimisation of perovskite film preparation:

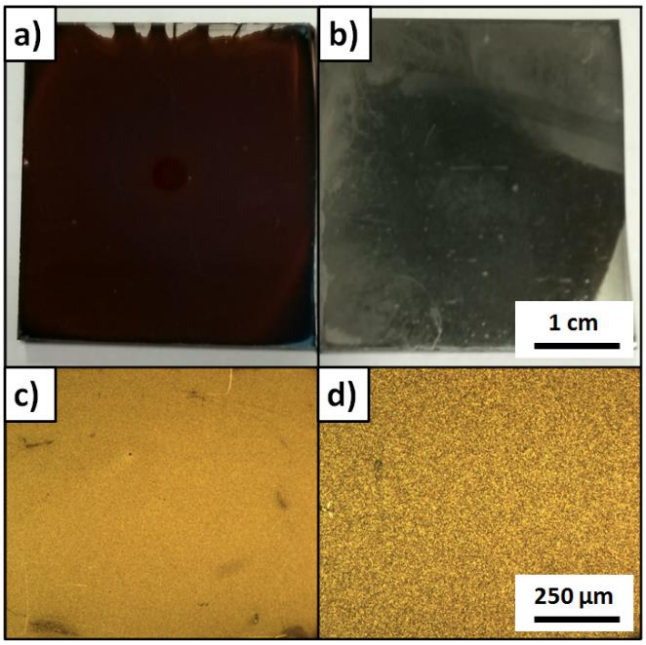

SI Figure 2. Photographs (a,b) and microscopic observations (c,d) of $CH_3NH_3PbI_3$ films spun on a 50 spray ETL; effect of ethyl acetate (a&c) vs. toluene (b&d) anti-solvent method.

Two different anti-solvents, ethyl acetate [44] vs. toluene [43] were tested in our laboratories where the perovskite films were spin-coated and solvent-treated in ambient conditions at relatively high humidity 55-65% RH. Visual and optical microscope observations of the $CH_3NH_3PbI_3$ films obtained after crystallisation (100 °C, 10mins) are shown in SI Figure 2. These images confirm the complete crystallization of the films and no apparent sign of degradation. Whilst the ethyl acetate modified films had a shiny mirror finish (SI Figure 2a), the toluene modified films displayed an opaque greyish appearance (SI Figure 2b). Microscopic observations confirmed these differences: while ethyl acetate-modified $CH_3NH_3PbI_3$ films (SI Figure 2c) displayed homogenous coverage, toluene-modified films (SI Figure 2d) were characterised with large isolated crystals. Following this optimisation study, all PSCs were prepared using the ethyl acetate anti-solvent method. Perovskite films prepared on 0-50 spray ETLs for device fabrication invariably displayed a smooth dark brown finish, as illustrated in Figure 7a.

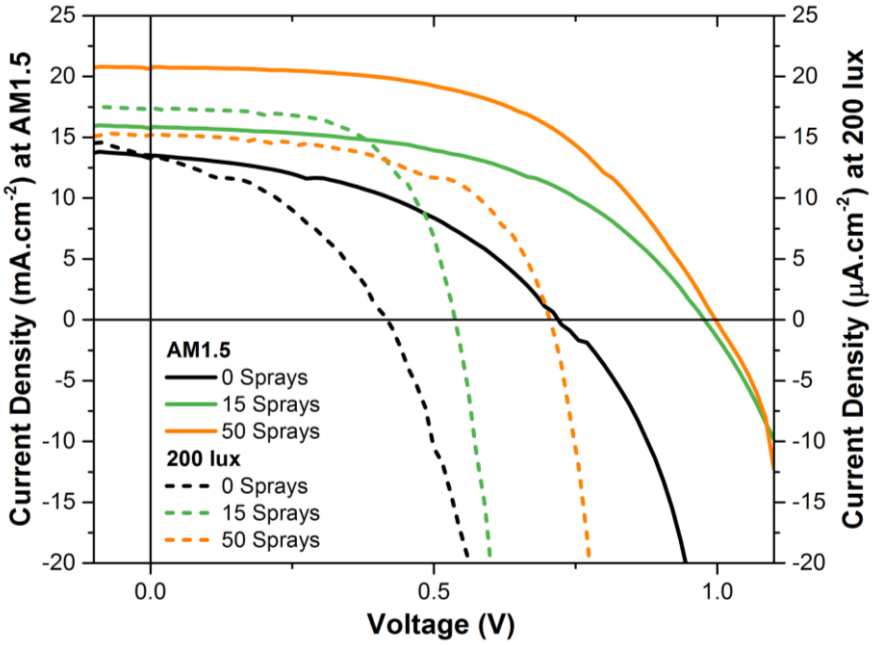

SI Figure 3. Comparative I/V data collected at AM1.5 and 200 lux illumination in reverse scan (V_{oc} to J_{sc}) for devices built on 0, 15, and 50 Sprays ETLs.

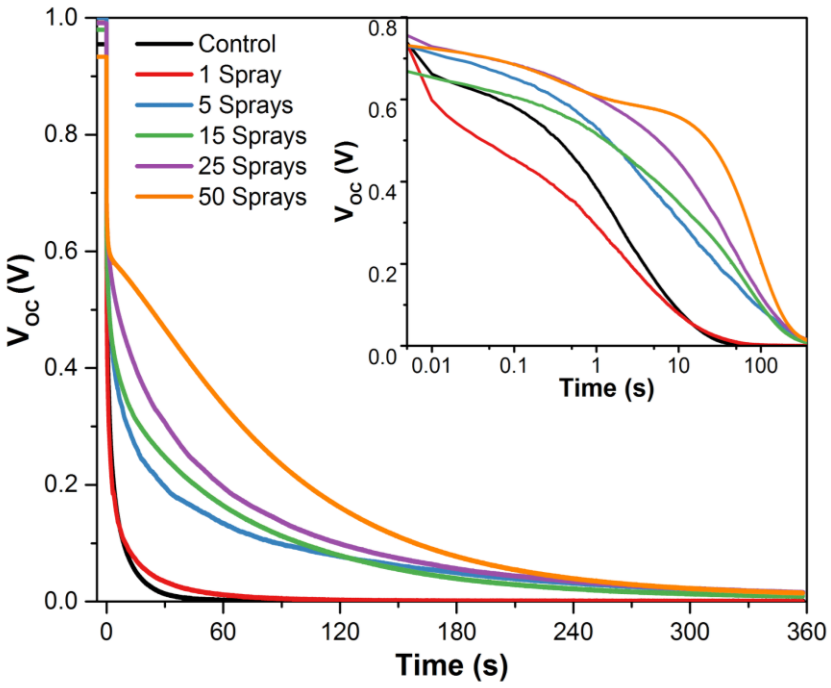

SI Figure 4. Open circuit voltage decay data collected for PSCs built on 0-50 spray ETLs.

Open circuit voltage data collected for PSCs built on 0-50 sprays ETLs are presented in SI Figure 4. All decays display a 2-stage evolution with a very fast decay from the V_{oc} to ~ 0.6 V within the first second, followed by a slower component from ~ 0.6 V to 0 V lasting between ~ 50-360s. The first stage of the decay is dominated by recombination of electrons and holes within the perovskite layer [62,63] and only very little impact of the ETL is observed (SI Figure 4, insert). The slower component of the decay is greatly affected by the structural properties of the ETL: slower decays are observed for devices built on ETLs prepared with increasing number of sprays. This can be attributed to a decrease in the density of pinholes in the TiO_2 ETL which act as recombination sites, in good agreement with cyclic voltammetry data shown in Figure 3.